Relativistic ionization probabilities and photoelectron distributions of hydrogenlike ions in superstrong electromagnetic fields

Dmitry A. Telnov [1,*] and Shih-I Chu [2,3,†]

[1] *Department of Physics, St. Petersburg State University, 7-9 Universitetskaya nab., St. Petersburg 199034, Russia*

[2] *Center for Quantum Science and Engineering, Department of Physics, National Taiwan University, Taipei 10617, Taiwan*

[3] *Department of Chemistry, University of Kansas, Lawrence, Kansas 66045, USA*

(Received 14 July 2021; accepted 12 August 2021; published 26 August 2021)

The ionization probabilities and photoelectron distributions of the hydrogen atom and hydrogenlike ions He^+ and Ne^{9+} in superstrong electromagnetic fields are obtained by solving the time-dependent Dirac equation with the help of the generalized pseudospectral method in spherical coordinates. A simple transformation of the original radial Dirac Hamiltonian is suggested that removes the spurious states. The ionization probabilities are calculated both within and beyond the dipole approximation for two pulse durations and various peak field strengths scaled with respect to the nuclear charge for each target. Performance of two analytic parameters previously suggested to estimate the nondipole effects is assessed against the numerical data obtained in this study. The photoelectron energy and angular distributions exhibit the above-threshold ionization peaks as well as the low-energy structure. In the superstrong field regime, the low-energy structure builds up with increasing field strength while the above-threshold ionization peaks decrease. The nondipole effects in the photoelectron distributions are also revealed and analyzed.

DOI: 10.1103/PhysRevA.104.023111

I. INTRODUCTION

Recent achievements in the laser technologies make it possible to generate extremely intense short pulses of coherent radiation thus attracting much interest to the light-matter interaction phenomena both in theory and experiment (see review papers [1,2] and references therein). The most powerful free-electron laser facilities, such as the European X-ray Free-Electron Laser facility (XFEL) [3] at Hamburg and the Linac Coherent Light Source (LCLS) [4] at Stanford, are expected to produce electromagnetic fields with extremely high brilliance and wavelengths down to 0.05 nm, giving opportunities to explore interaction of strong and short-wavelength electromagnetic fields with highly charged ions in the relativistic domain. On the other hand, the relativistic regime can be reached with optical lasers at intensities higher than 10^{17} W/cm^2, where electrons can reach relativistic velocities within one optical cycle. New interesting phenomena, such as relativistic self-focusing in plasmas, relativistic multiphoton and tunneling recollision dynamics, laser-assisted electron-positron pair production, etc., can be possibly observed [2].

Theoretical and computational studies of atomic and molecular systems exposed to electromagnetic fields with extremely high intensities must be relativistic since the electron moves with a very high speed under the influence of both the strong external electromagnetic field and Coulomb field of the nuclei. Various approaches have been suggested so far to serve the purpose. There are several methods to solve the time-dependent Dirac equation (TDDE) numerically in spherical coordinates with expansion of the angular part of the wave function in spherical harmonics [5–10]. The radial wave function can be either discretized on the exponential mesh [5,11] or expanded on a basis of B splines [6–10]. Kinetically balanced B-spline basis sets in both radial and angular coordinates for the TDDE with an axial symmetry were used in Ref. [12]. Complex rotation of the coordinates [5,7] and complex absorbing potentials [8,9] were applied as well. Other theoretical and computational approaches feature the relativistic time-dependent close-coupling method [13,14], relativistic generalization of the matrix iteration method [15,16], and classical relativistic phase-space averaging method, generalized to arbitrary central potentials [17]. The relativistic Coulomb-corrected strong-field approximation [18,19] has been used for treatment of above-threshold ionization. We can also mention the recently developed approaches dealing with Schrödinger-like equations [20–22].

For the wavelength of the external electromagnetic field exceeding the atomic size to a great extent, the electric dipole approximation has been a common approach to describe the interaction of the atom or ion with the field. In the dipole approximation, the variation of the vector potential in space is neglected; then the external field is a time-dependent and spatially uniform electric field, while the magnetic field totally vanishes. However, nondipole effects due to magnetic fields may be important even at long wavelengths, depending on the field intensity [23–25]. When the intensity of the laser field increases, so does the velocity of the rescattering electron. Then the nondipole effects due to the magnetic field of the laser pulse become more and more important, and the dipole approximation eventually breaks down.

*d.telnov@spbu.ru

†sichu@ku.edu

A breakdown of the dipole approximation was observed experimentally in mid-infrared [26,27] and near-infrared [28] laser fields. Description of the interaction with the external electromagnetic field beyond the dipole approximation may be necessary even if an atomic or molecular system is treated nonrelativistically with the time-dependent Schrödinger equation (TDSE) [29–32]. For relativistic atomic and molecular systems, various approaches were suggested to extend the treatment beyond the dipole approximation in the TDDE [5,7–9,14,16,33,34]. They include the Fourier [5], power series [8], spherical Bessel function [14], and spherical harmonics [16] expansions as well as the spatial grid representation of the nondipole vector potential [33,34] to accommodate the nondipole corrections.

In our previous work, we applied the generalized pseudospectral (GPS) method to solve the TDDE and studied ionization of relativistic diatomic quasimolecules [33] and hydrogenlike ions [34] in strong electromagnetic fields. For the diatomic quasimolecules, the GPS discretization was performed in prolate spheroidal coordinates, which represent the natural choice for two-center systems. In this case, we found that spurious states do not emerge among the true bound states when solving the discretized Dirac eigenvalue problem [33]. For the hydrogenlike ions, spherical coordinates are the natural choice of coordinate system. Previously, the GPS method in spherical coordinates was successfully applied to a number of nonrelativistic atomic problems (see Ref. [35] and references therein). This method does not require computations of the potential energy matrix elements, and its nonuniform spatial grid is well suited for treatment of the systems bound by the Coulomb forces. When solving the eigenvalue problem, highly accurate results can be obtained with a moderate number of grid points. Therefore, it was desirable to extend this method to relativistic atomic systems described by the Dirac equation. However, straightforward application of the GPS method in spherical coordinates to the Dirac eigenvalue problem is unsuccessful because the spurious states do appear, and they may interfere in solving the TDDE as well. In our recent paper [34], we suggested a modification of the discretized Dirac Hamiltonian in spherical coordinates that removes the spurious states while maintaining a high accuracy of the true bound states. The method of Ref. [34] was formulated for the Dirac Hamiltonian discretized on a two-dimensional (2D, r and ϑ) grid, only the azimuthal angle φ was separated from the very beginning. The resulting matrix problem is quite large in size, making the TDDE calculations beyond the dipole approximation time consuming. However, in the central force field, the eigenvalue problem can be recast in the form of the one-dimensional (1D) radial Dirac equation, thus drastically reducing the computational effort. In the present paper, we address this issue and suggest a modification of the radial Dirac Hamiltonian based on the ideas of Ref. [34], which removes the spurious states. Then the method is applied for calculations of the ionization probabilities of the hydrogen atom as well as hydrogenlike ions He^+ and Ne^{9+} in superstrong electromagnetic field both within and beyond the dipole approximation. Conclusions are made about applicability of the dipole approximation. We also calculate and analyze the photoelectron energy and angle distributions.

The paper is organized as follows. In Sec. II, we present theoretical and computational details of our approach. Here we suggest a modification of the radial Hamiltonian matrix, which removes the spurious states, and outline the time-propagation procedure for the TDDE. In Sec. III, we present and discuss our results regarding relativistic ionization dynamics of hydrogenlike ions in superstrong electromagnetic fields. In Sec. III A, we study the dependence of the ionization probabilities on the peak field strength and pulse duration and draw conclusions about applicability of the dipole approximation. In Sec. III B, we present and analyze the photoelectron distributions with respect to the energy and emission angle. Section IV contains concluding remarks. Atomic units (a.u.) are used throughout the paper unless specified otherwise.

II. THEORETICAL AND COMPUTATIONAL METHODS

A. Time-dependent Dirac equation for one-electron system in linearly polarized electromagnetic field

To obtain the ionization probability and distributions of emitted electrons, one has to solve the time-dependent Dirac equation:

$$i\frac{\partial}{\partial t}\Psi(\boldsymbol{r},t) = (H_0 + V)\Psi(\boldsymbol{r},t), \tag{1}$$

where $\Psi(\boldsymbol{r},t)$ is a four-component wave function, V represents interaction with the external electromagnetic field, and H_0 is the unperturbed Dirac Hamiltonian of the electron moving in the central force field of the atomic nucleus:

$$H_0 = c(\boldsymbol{\alpha}\cdot\boldsymbol{p}) + m_e c^2\beta + U(r). \tag{2}$$

In Eq. (2), c is the speed of light, $\boldsymbol{p}$ is the momentum operator, m_e is the electron mass ($m_e = 1$ in atomic units), and $U(r)$ is the nucleus potential. We make use of the Dirac matrices $\boldsymbol{\alpha}$ and β in the standard representation [36]

$$\boldsymbol{\alpha} = \begin{bmatrix} 0_2 & \boldsymbol{\sigma} \\ \boldsymbol{\sigma} & 0_2 \end{bmatrix}, \quad \beta = \begin{bmatrix} 1_2 & 0_2 \\ 0_2 & -1_2 \end{bmatrix}, \tag{3}$$

where "0_2" and "1_2" are the zero and unit 2×2 matrices, respectively,

$$0_2 = \begin{pmatrix} 0 & 0 \\ 0 & 0 \end{pmatrix}, \quad 1_2 = \begin{pmatrix} 1 & 0 \\ 0 & 1 \end{pmatrix}, \tag{4}$$

and the vector $\boldsymbol{\sigma}$ consists of the Pauli matrices as components. We assume that the external electromagnetic field is linearly polarized along the z axis; it is described by the vector potential

$$\boldsymbol{A}(\boldsymbol{r},t) = A(\boldsymbol{r},t)\hat{\boldsymbol{z}}, \tag{5}$$

where $\hat{\boldsymbol{z}}$ is the unit vector along the z axis. Then the interaction term V in Eq. (1) takes the form

$$V(\boldsymbol{r},t) = A(\boldsymbol{r},t)\begin{bmatrix} 0_2 & \sigma_z \\ \sigma_z & 0_2 \end{bmatrix} \tag{6}$$

with σ_z being the standard Pauli matrix:

$$\sigma_z = \begin{pmatrix} 1 & 0 \\ 0 & -1 \end{pmatrix}. \tag{7}$$

To solve problem (1), in our previous paper [34] we applied the generalized pseudospectral discretization to both the radial

coordinate r and polar angle ϑ. The resulting Hamiltonian matrices have a rather large dimension equal to the product of the r and ϑ grid point numbers. In the present study, we make use of the wave function expansion on the basis of the spherical spinors and discretize the radial coordinate only. Thus we can greatly reduce the dimension of the Hamiltonian matrices and speed up the computations.

We use the following definition of the spherical spinors [37]:

$$\Omega_{\kappa m} = \begin{Vmatrix} \sqrt{\dfrac{|\kappa|+m}{2|\kappa|-1}}\, Y_{|\kappa|-1,m} \\ \sqrt{\dfrac{|\kappa|-m-1}{2|\kappa|-1}}\, Y_{|\kappa|-1,m+1} \end{Vmatrix} \quad (\kappa < 0),$$

$$\Omega_{\kappa m} = \begin{Vmatrix} -\sqrt{\dfrac{\kappa-m}{2\kappa+1}}\, Y_{\kappa,m} \\ \sqrt{\dfrac{\kappa+m+1}{2\kappa+1}}\, Y_{\kappa,m+1} \end{Vmatrix} \quad (\kappa > 0), \tag{8}$$

where $Y_{lm}(\vartheta, \varphi)$ is the spherical function for the orbital angular momentum l and its projection m on the z axis. An integer number κ is expressed through the total angular momentum j and orbital angular momentum l:

$$\kappa = l(l+1) - j(j+1) - 1/4. \tag{9}$$

Since $l = j \pm 1/2$, the number κ spans the whole integer range except zero. If $l = j - 1/2$, then $\kappa = -l - 1$; otherwise, if $l = j + 1/2$, then $\kappa = l$. The spherical spinors $\Omega_{\kappa m}$ constitute an orthonormal and complete set of two-component functions depending on the angles ϑ and φ. Consequently, both the upper and lower two-component parts of the four-component wave function $\Psi(\boldsymbol{r}, t)$ can be expanded on this basis set. We use the following representation of the wave function:

$$\Psi(\boldsymbol{r}, t) = \frac{1}{r} \sum_{\kappa m} \begin{bmatrix} f_{\kappa m}(r,t)\Omega_{\kappa m} \\ i g_{\kappa m}(r,t)\Omega_{-\kappa m} \end{bmatrix}. \tag{10}$$

Here the lower expansion coefficient $g_{\kappa m}(r, t)$ is multiplied by i for convenience. If the expansion of the wave function is used in the form (10), only the functions $f_{\kappa m}(r, t)$ and $g_{\kappa m}(r, t)$ with the same κ and m are coupled by the unperturbed Hamiltonian H_0. The following relation holds:

$$H_0\Psi = \frac{1}{r} \sum_{\kappa m} \begin{bmatrix} \Omega_{\kappa m} & 0 \\ 0 & i\Omega_{-\kappa m} \end{bmatrix} \times H_0^{(\kappa)} \begin{bmatrix} \langle\Omega_{\kappa m}| & 0 \\ 0 & -i\langle\Omega_{-\kappa m}| \end{bmatrix} r\Psi. \tag{11}$$

The bra notation in the matrices on the right-hand side of Eq. (11) is used to emphasize that the inner product in the space of two-component functions of angular coordinates is taken when these matrices act upon the four-component wave function $r\Psi$, so the results are two-component radial wave functions:

$$\begin{bmatrix} \langle\Omega_{\kappa m}| & 0 \\ 0 & -i\langle\Omega_{-\kappa m}| \end{bmatrix} r\Psi = \begin{pmatrix} f_{\kappa m} \\ g_{\kappa m} \end{pmatrix}. \tag{12}$$

The latter functions are then acted upon by the radial Hamiltonians $H_0^{(\kappa)}$, which are 2×2 matrices:

$$H_0^{(\kappa)} = T_\kappa + U(r) \begin{pmatrix} 1 & 0 \\ 0 & 1 \end{pmatrix}, \tag{13}$$

T_κ being the kinetic and rest energy operator,

$$T_\kappa = m_e c^2 \begin{pmatrix} 1 & \dfrac{B_\kappa}{m_e c} \\ \dfrac{B_\kappa^\dagger}{m_e c} & -1 \end{pmatrix}. \tag{14}$$

Here the operator B_κ is defined as follows:

$$B_\kappa = -\frac{d}{dr} + \frac{\kappa}{r}, \quad B_\kappa^\dagger = \frac{d}{dr} + \frac{\kappa}{r}. \tag{15}$$

The time propagation in Eq. (1) is performed with the help of the split-operator method in the energy representation [38]. Previously, we used this method to solve the TDSE [39–41] and time-dependent Kohn-Sham equations [42–44]. In the TDDE, we applied this method previously for quasimolecules in prolate spheroidal coordinates [33] and hydrogenlike ions in spherical coordinates [34]. The split-operator form of the short-time propagator is as follows:

$$\Psi(t + \Delta t) = \exp\left(-\frac{i}{2}\Delta t\, H_0\right) \times \exp\left[-i\Delta t\, V\left(t + \frac{1}{2}\Delta t\right)\right] \times \exp\left(-\frac{i}{2}\Delta t\, H_0\right)\Psi(t). \tag{16}$$

An error bound of this scheme is of the order of $(\Delta t)^3$. Since the field-free propagator $\exp(-\frac{i}{2}\Delta t\, H_0)$ is time independent, it is calculated only once for the chosen time step Δt. In the previous implementation [34], the propagator matrices were constructed on a 2D (r and ϑ) grid for each angular momentum projection m and had large dimensions. For example, the dimension of the propagator matrix is equal to 8192 if 128 radial and 16 angular (ϑ) grid points are used. With such large matrices, matrix-vector multiplications in the propagation process are very time consuming. In the present implementation, we make use of 1D radial propagators for each κ, so the field-free short-time propagator takes a form similar to that in Eq. (11):

$$\exp\left(-\frac{i}{2}\Delta t\, H_0\right) = \frac{1}{r} \sum_{\kappa m} \begin{bmatrix} \Omega_{\kappa m} & 0 \\ 0 & i\Omega_{-\kappa m} \end{bmatrix} \exp\left(-\frac{i}{2}\Delta t\, H_0^{(\kappa)}\right) \times \begin{bmatrix} \langle\Omega_{\kappa m}| & 0 \\ 0 & -i\langle\Omega_{-\kappa m}| \end{bmatrix} r. \tag{17}$$

The partial propagators $\exp(-\frac{i}{2}\Delta t\, H_0^{(\kappa)})$ are calculated by the spectral expansion

$$\exp\left(-\frac{i}{2}\Delta t\, H_0^{(\kappa)}\right) = \sum_n \exp\left(-\frac{i}{2}\Delta t\, E_n^{(\kappa)}\right) |\psi_n^{(\kappa)}\rangle\langle\psi_n^{(\kappa)}|, \tag{18}$$

where the two-component radial wave functions $\psi_n^{(\kappa)}(r)$ are the eigenstates of the radial Hamiltonians $H_0^{(\kappa)}$ corresponding

to the energy eigenvalues $E_n^{(\kappa)}$:

$$H_0^{(\kappa)}\psi_n^{(\kappa)}(r) = E_n^{(\kappa)}\psi_n^{(\kappa)}(r). \tag{19}$$

The field-free propagator representation (17) is very useful since it allows to use several matrices of a smaller dimension (partial propagators) rather than one matrix of a larger dimension (full propagator) in the matrix-vector multiplication.

The external field propagator $\exp(-i\Delta t V)$ has an analytic expression for the interaction operator given by Eq. (6):

$$\exp(-i\Delta t V) = \begin{bmatrix} \cos(A\Delta t)1_2 & -i\sin(A\Delta t)\sigma_z \\ -i\sin(A\Delta t)\sigma_z & \cos(A\Delta t)1_2 \end{bmatrix}. \tag{20}$$

In the full grid representation [where all the coordinates are discretized on a three-dimensional (3D) grid], matrix (20) is quasidiagonal in the sense that it consists of four square blocks, each of them being a diagonal matrix (note that multiplication by a function of the coordinates is represented by a diagonal matrix in the GPS method). The field propagator matrix is time dependent and must be computed at each time step. This computation is not time consuming, however, since the matrix is quasidiagonal.

The external field propagator (20) couples the positive and negative energy states of the unperturbed Dirac Hamiltonian with the large energy gap $2m_e c^2$ between them. Therefore, the time step Δt in the split-operator method must be small enough to preserve the accuracy of the calculations. Generally, Δt must be much smaller than that in the similar TDSE calculations. This issue is well known for the TDDE and has been discussed in the literature [8,15,45]. In our calculations of the hydrogen atom, converged results in the TDDE propagation using the split-operator method can be obtained with the time step about two orders of magnitude smaller than the time step in the TDSE propagation for the same atom and field parameters.

At every time step, the external field propagator (20) is applied to the wave function in the full grid representation while the field-free propagator (17) requires the wave function expansion on the basis of spherical spinors (10) where only the radial functions have grid representations. To obtain the radial functions $f_{\kappa m}(r,t)$ and $g_{\kappa m}(r,t)$ from the full grid representation of the wave function $\Psi(\boldsymbol{r},t)$, we invert Eq. (10):

$$\begin{pmatrix} f_{\kappa m} \\ g_{\kappa m} \end{pmatrix} = \begin{bmatrix} \langle\Omega_{\kappa m}| & 0 \\ 0 & -i\langle\Omega_{-\kappa m}| \end{bmatrix} r\Psi(\boldsymbol{r},t). \tag{21}$$

The inner product in the space of two-component functions of angular coordinates on the right-hand side of Eq. (21) assumes integration with respect to the coordinates ϑ and φ. The azimuthal angle φ is discretized on a uniform grid in the range $[0, 2\pi]$. The number of the φ grid points is equal to the number of angular momentum projections retained in the wave function. Then the integration with respect to this coordinate is performed using computer-optimized fast Fourier transform routines. The polar angle ϑ is discretized with the help of the Gauss-Legendre pseudospectral method, and the corresponding quadrature abscissas and weights are used to perform integration.

B. Generalized pseudospectral discretization of the radial Dirac Hamiltonian and removal of spurious states

To solve the radial eigenvalue problem (19), we discretize the radial coordinate r using the GPS method [34,43]. We apply the Gauss-Lobatto scheme where the collocation points are the roots of the following equation:

$$(1-x^2)P'_{N_x+1}(x) = 0, \tag{22}$$

with $P'_{N_x+1}(x)$ being the derivative of the Legendre polynomial. The variable x is mapped to the coordinate r according to the transformation [34,43]

$$r(x) = R_m \frac{(1+x)^2 + 2\delta(1+x)}{1-x+4R_m(1+\delta)/R_b}. \tag{23}$$

The collocation points -1 and 1 are mapped to $r=0$ and $r=R_b$, respectively. If zero boundary conditions are imposed on the wave function at these points, only N_x internal collocations points are used to represent the discretized wave function. The end point R_b must be chosen large enough so the electron driven by the Coulomb and external field forces fit in the spatial box. The parameters R_m and δ can be used to adjust the distribution of the radial grid points within the interval $[0, R_b]$. In particular, smaller values of the parameter δ make the distribution denser in the vicinity of the nucleus; this is necessary in the calculations of heavy ions where the extended nucleus model is used.

It is convenient to introduce arrays $\phi_{i\kappa m}$ and $\chi_{i\kappa m}$ containing the scaled values of the functions $f_{\kappa m}$ and $g_{\kappa m}$, respectively, at the grid points r_i:

$$\begin{aligned} f_{\kappa m}(r_i) &= \sqrt{\frac{(N_x+1)(N_x+2)}{2r'_i}} \\ &\quad \times P_{N_x+1}(x_i)\phi_{i\kappa m}, \\ g_{\kappa m}(r_i) &= \sqrt{\frac{(N_x+1)(N_x+2)}{2r'_i}} \\ &\quad \times P_{N_x+1}(x_i)\chi_{i\kappa m} \end{aligned} \tag{24}$$

(r'_i denote the values of the derivatives dr/dx at the collocation points x_i). Then the normalization integral of the wave function is calculated as follows:

$$\int d^3r[\Psi(\boldsymbol{r})]^\dagger\Psi(\boldsymbol{r}) = \sum_{\kappa m}\sum_{i=1}^{N_x}(|\phi_{i\kappa m}|^2 + |\chi_{i\kappa m}|^2). \tag{25}$$

Upon discretization, the first derivative operator with respect to the radial coordinate in the operator B_κ [Eq. (15)] is represented by a matrix acting upon the vector with the components $\phi_{i\kappa m}$ or $\chi_{i\kappa m}$. The matrix elements are calculated according to the equation

$$\left(\frac{d}{dr}\right)_{ii'} = \frac{d^x_{ii'}}{\sqrt{r'_i r'_{i'}}}, \tag{26}$$

where $d^x_{ii'}$ is defined as follows:

$$d^x_{ii'} = \frac{1}{x_i - x_{i'}} \ (i \neq i'), \quad d^x_{ii} = 0 \ (1 \leqslant i \leqslant N_x). \tag{27}$$

The nuclear potential and other multiplications by functions of the coordinate r in the Hamiltonian are represented by

diagonal matrices in the GPS method, with the matrix elements equal to the values of the potential at the collocation points.

It is commonly known that solving the eigenvalue problem for the Dirac equation using basis-set expansions leads to emergence of spurious eigenstates [46]. Various techniques were implemented to remove such undesirable states, from imposing special boundary conditions [47,48] to working with kinetically balanced basis sets [49]. When using B splines, it was shown that spurious states are eliminated if splines of different order are applied to approximate the large and small components of the wave function [50]. Other numerical schemes, which are based on B splines and free from the spurious states, were discussed in Ref. [51]. It was reported [52] that the split-shift potential method for the radial Dirac equation does not generate the spurious states either. The spurious states do not show up, at least among the low-lying bound states, when the Dirac eigenvalue problem is solved with the help of the GPS method in prolate spheroidal coordinates [33]. When the GPS method is applied to the central-force-field Dirac eigenvalue problem in spherical coordinates, the spurious states do exist. Previously, using the ideas of the dual kinetic balance (DKB) approach [49], we suggested a transformation of the discretized Hamiltonian, upon which the spurious states are removed [34]. The procedure [34] is applied to the Dirac Hamiltonian matrix discretized by the GPS method on a 2D (r and ϑ) grid. Here we describe a simpler transformation intended for the 1D radial Dirac Hamiltonian. First, the following substitution is applied for the radial wave function:

$$\begin{pmatrix} f_{\kappa m} \\ g_{\kappa m} \end{pmatrix} = Q_\kappa \begin{pmatrix} \tilde{f}_{\kappa m} \\ \tilde{g}_{\kappa m} \end{pmatrix}, \quad \psi_n^{(\kappa)} = Q_\kappa \tilde{\psi}_n^{(\kappa)}, \tag{28}$$

where the matrix Q_κ is defined as follows:

$$Q_\kappa = \begin{pmatrix} 1 & -\dfrac{B_\kappa}{2m_e c} \\ \dfrac{B_\kappa^\dagger}{2m_e c} & 1 \end{pmatrix}. \tag{29}$$

To make the radial eigenvalue problem symmetric, Eq. (19) should be also multiplied by $Q_\kappa^\dagger$:

$$Q_\kappa^\dagger H_0^{(\kappa)} Q_\kappa \tilde{\psi}_n^{(\kappa)} = E_n^{(\kappa)} Q_\kappa^\dagger Q_\kappa \tilde{\psi}_n^{(\kappa)}. \tag{30}$$

In particular, the kinetic and rest energy part of the Hamiltonian T_κ is transformed as follows:

$$Q_\kappa^\dagger T_\kappa Q_\kappa = m_e c^2 \begin{pmatrix} 1 + \dfrac{3B_\kappa B_\kappa^\dagger}{(2m_e c)^2} & -\dfrac{2B_\kappa B_\kappa^\dagger B_\kappa}{(2m_e c)^3} \\ -\dfrac{2B_\kappa^\dagger B_\kappa B_\kappa^\dagger}{(2m_e c)^3} & -1 - \dfrac{3B_\kappa^\dagger B_\kappa}{(2m_e c)^2} \end{pmatrix}. \tag{31}$$

Of course, if the discretized $H_0^{(\kappa)}$ and Q_κ matrices of finite dimension are used in Eq. (30), then the transition from Eq. (19) to Eq. (30) is done by matrix multiplication only and does not change the eigenvalues, so the spurious states are still present. The key point of the procedure is a *modification* of the T_κ matrix that actually removes the spurious states. This is achieved by calculation of the operator products $B_\kappa B_\kappa^\dagger$ and $B_\kappa^\dagger B_\kappa$ on the diagonal of the matrix in Eq. (31) analytically *before* the discretization is applied:

$$B_\kappa B_\kappa^\dagger = -\frac{d^2}{dr^2} + \frac{\kappa(\kappa+1)}{r^2},$$
$$B_\kappa^\dagger B_\kappa = -\frac{d^2}{dr^2} + \frac{\kappa(\kappa-1)}{r^2}. \tag{32}$$

Proper discretized forms of these operators read as

$$(B_\kappa B_\kappa^\dagger)_{ii'} = \frac{1}{\sqrt{r_i' r_{i'}'}} \sum_{k=0}^{N_x+1} \frac{d_{ki}^x d_{ki'}^x}{r_k'} + \frac{\kappa(\kappa+1)}{r_i^2}\delta_{ii'},$$
$$(B_\kappa^\dagger B_\kappa)_{ii'} = \frac{1}{\sqrt{r_i' r_{i'}'}} \sum_{k=0}^{N_x+1} \frac{d_{ki}^x d_{ki'}^x}{r_k'} + \frac{\kappa(\kappa-1)}{r_i^2}\delta_{ii'}. \tag{33}$$

They cannot be obtained by simple matrix multiplication of the discretized B_κ and $B_\kappa^\dagger$. First, note that summation on the right-hand side of Eq. (33) includes the end points $k = 0$ and $k = N_x + 1$. These points are not used in the first derivative matrix (26) due to the zero boundary conditions imposed on the wave function. However, the zero boundary conditions at $r = 0$ and $r = R_b$ may not be satisfied by the first derivative of the wave function, and the end points must be included when the subsequent differentiation is performed. Second, the centrifugal terms in Eq. (32) cannot be correctly reproduced either when taking a matrix product of discretized B_κ and $B_\kappa^\dagger$.

We note that it is sufficient to substitute the result (33) on the diagonal of the transformed rest and kinetic energy (31) only; the off-diagonal elements can be calculated by matrix multiplication with the discretized B_κ and $B_\kappa^\dagger$. Upon this modification of the Hamiltonian, spurious states disappear when the eigenvalue problem (30) is solved. However, Eq. (30) represents not a standard but a generalized eigenvalue problem, making it somewhat inconvenient to solve the time-dependent problems since the eigenstates are not orthogonal. To avoid possible complications, we now revert the transformations of the wave function and Hamiltonian with the matrix Q_κ^{-1} obtained by inversion of the *discretized* matrix Q_κ and arrive at a standard eigenvalue problem similar to that in Eq. (19):

$$\bar{H}_0^{(\kappa)} \psi_n^{(\kappa)}(r) = E_n^{(\kappa)} \psi_n^{(\kappa)}(r) \tag{34}$$

with the Hamiltonian $\bar{H}_0^{(\kappa)}$ defined as

$$\bar{H}_0^{(\kappa)} = \bar{T}_\kappa + U(r) \begin{pmatrix} 1 & 0 \\ 0 & 1 \end{pmatrix}. \tag{35}$$

While the potential term in Eq. (35) is the same as in the original Hamiltonian (13), the rest and kinetic energy matrix $\bar{T}_\kappa$ differs from the discretized version of the original operator (14). After the transformations described above, the Hamiltonian $\bar{H}_0^{(\kappa)}$ is modified from its original form $H_0^{(\kappa)}$. Compared to the directly discretized original eigenvalue problem (19), Eq. (34) returns accurate physical eigenstates but no spurious states.

III. RESULTS AND DISCUSSION

We have performed calculations of the ionization probabilities and photoelectron energy and angular distributions for the hydrogen atom and two hydrogenlike ions, He^+ and Ne^{9+}, subject to strong pulses of electromagnetic radiation. For these

light atomic systems, the effect of the finite nuclear size on the electronic structure and dynamics is insignificant, and we use a pointlike nucleus model with the exact Coulomb interaction between the electron and the nucleus:

$$U(r) = -\frac{Z}{r}, \tag{36}$$

Z being the nuclear charge. Interaction with the external electromagnetic field is described by Eqs. (6) and (5). The field is linearly polarized along the z axis and propagates along the x axis; we adopt the Gaussian shape of the laser pulse:

$$A(\boldsymbol{r}, t) = \frac{cF}{\omega} \exp\left[-2\ln 2\left(\frac{t - x/c}{\tau}\right)^2\right] \times \sin\left(\omega t - \frac{\omega x}{c}\right), \tag{37}$$

where F is the peak electric field strength, ω is the carrier frequency, and τ has a meaning of the full width at half maximum (FWHM) in the A^2 (intensity) profile. Equation (37) describes the general case beyond the dipole approximation. In the dipole approximation, the dependence of the vector potential on the coordinate x is dropped:

$$A(t) = \frac{cF}{\omega} \exp\left[-2\ln 2\left(\frac{t}{\tau}\right)^2\right] \sin\omega t. \tag{38}$$

It is well known that nonrelativistic Coulomb systems satisfy exact scaling relations with respect to the nuclear charge Z. The unperturbed ($F = 0$) electronic energy eigenvalues of the hydrogenlike ions with different Z scale as Z^2 but the scaling laws hold also for the ions interacting with external electromagnetic fields in the dipole approximation [53]. A proper scaling of the spatial and time variables as well as pulse parameters in the TDSE converts the equation for the ion with the nuclear charge Z into the equation for the hydrogen atom ($Z = 1$). This nonrelativistic scaling is achieved by the following transformation:

$$\boldsymbol{r} = \tilde{\boldsymbol{r}}Z^{-1}, \quad t = \tilde{t}Z^{-2}, \quad \omega = \tilde{\omega}Z^2, \quad \tau = \tilde{\tau}Z^{-2}, \quad F = \tilde{F}Z^3, \tag{39}$$

where the variables and parameters with tilde correspond to the H atom. The ionization probabilities are equal to each other for all hydrogenlike ions if the interaction with the external field is described within the dipole approximation (38) and the pulse parameters are scaled according to Eqs. (39). These rules do not apply to relativistic systems described by the TDDE, although some approximate scaling relations have been suggested [6,10]. Then any differences between the ionization probabilities obtained by solving the TDDE for the systems scaled according to Eqs. (39) (within the dipole approximation) may be attributed to relativistic effects, which are expected to grow with the increase of the nuclear charge Z. As discussed in Ref. [6] for multiphoton ionization of hydrogenlike ions, the main effect is the downshift of the ground-state energy level in the relativistic case resulting in somewhat smaller ionization probabilities obtained for the scaled systems with larger Z. If the interaction with the external field is described beyond the dipole approximation, the scaling law for the ionization probability does not hold either.

For the hydrogen atom and light hydrogenlike ions studied in this paper ($Z = 1, Z = 2$, and $Z = 10$), we perform the GPS discretization of the radial coordinate and apply Eq. (23) with the following values of the parameters:

$$R_m = 30Z^{-1}\,\text{a.u.}, \quad R_b = 100Z^{-1}\,\text{a.u.}, \quad \delta = 1. \tag{40}$$

For each target, the length parameters R_m and R_b are scaled according to Eqs. (39), while the dimensionless parameter δ remains unscaled. Using 160 radial grid points, we obtain the bound-state energies for the principal quantum numbers $n = 1$–4 with the relative error bound of 10^{-9}, as compared to the analytic Dirac Coulomb energies [36]. For higher-lying bound states, the eigenvalue accuracy gradually decreases; this is mainly because of the finite radial box size R_b where the problem is solved. When solving the TDDE, we include the states with $|\kappa| \leqslant 16$ in the expansion (10); as our calculations show, this is well in excess for the laser pulse parameters used in the present study. As to the angular momentum projection, $m = 0$ in the dipole approximation; beyond the dipole approximation, the m limits are adjusted in the expansion (10) to achieve convergence for each peak field value used in the calculations. To prevent spurious reflections of the electron wave packet from the box boundary, we use an absorbing layer in the vicinity of R_b.

A. Total ionization probabilities of hydrogenlike ions and breakdown of dipole approximation

The total ionization probabilities have been calculated for H, He^+, and Ne^{9+} both within and beyond the dipole approximation. For the H atom, the carrier frequency of the laser pulse in Eq. (37) is fixed at 3.5 a.u., the same frequency that was used in the recent studies of the relativistic ionization dynamics of the hydrogen atom [7,8,34]. The field strength range is 0–90 a.u. For the hydrogenlike ions He^+ and Ne^{9+}, the parameters have been scaled according to Eqs. (39). The spatial box used in the simulations ($R_b = 100Z^{-1}$ a.u.) is large enough to accommodate all ionization dynamics even at strongest fields in the range. For example, the classical excursion distance of the electron in the laser field can be estimated as F/ω^2; at $F = 90Z^3$ a.u., this quantity is equal to $7.35Z^{-1}$ a.u., which is well below R_b. Convergence with respect to the other numerical parameters was checked by performing test calculations with slightly changed parameters. We may conclude that the ionization probabilities have been calculated with an accuracy of about 1%.

The calculations are performed for two values of the pulse duration parameter τ in Eq. (37): 2.5 and 3.75 optical cycles (o.c.). Since the pulse shape is Gaussian, the pulse envelope function never turns zero, and the actual propagation time should be chosen appropriately, so the field strength is negligibly small at the beginning and end of the pulse. The actual propagation times for the values of the τ parameter listed above are 10 and 15 o.c., respectively. Finally, we use 65 536 time steps per optical cycle in the split-operator propagation method to make sure the results are converged with respect to this parameter. Before the external field is switched on, the target is in the ground state, and the ionization probability P_i

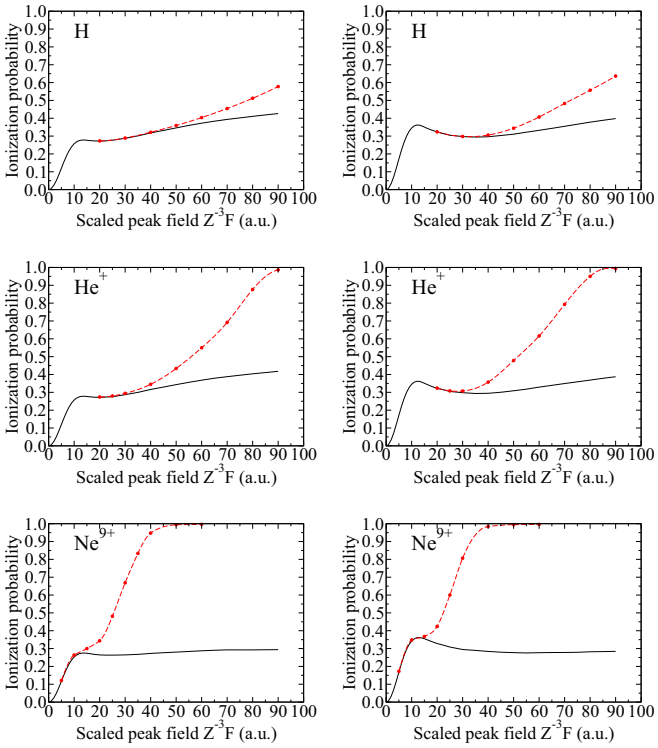

FIG. 1. Ionization probabilities of the hydrogenlike ions versus the peak field strength. The laser pulse is Gaussian with the carrier frequency $\omega = 3.5Z^2$ a.u. Left column, pulse duration $\tau = 2.5$ o.c.; right column, pulse duration $\tau = 3.75$ o.c. Top row, hydrogen atom; middle row, He^+; bottom row, Ne^{9+}. Black solid line, dipole approximation; red dashed line, beyond the dipole approximation. Red circles show the data points calculated beyond the dipole approximation.

is calculated as

$$P_i = 1 - P_b, \tag{41}$$

where P_b is the total population of bound states at the end of the time propagation. Figure 1 displays the ionization probabilities of the H atom, He^+, and Ne^{9+} versus the peak field strength both within and beyond the dipole approximation. Convergence of the nondipole results is achieved by increasing the number of angular momentum projections m in the wave function. For the weaker external fields, where the difference of the dipole and nondipole ionization probabilities is small, the convergence is reached at the level $|m| \leqslant 2$ already. However, for the strongest peak fields used in our calculations, we had to include the angular momentum projections $|m| \leqslant 11$ to obtain converged nondipole ionization probabilities.

If the external field is relatively weak, the dipole probabilities show a rapid increase with the field strength. This pattern ends around the scaled field peak value $F = 10Z^{-1}$ a.u., where the ionization probability curve has a local maximum followed by a shallow minimum. After that, the dipole ionization probability exhibits a slow increase or remains almost constant as the field gets stronger. Such a counterintuitive behavior of the ionization probability is known as stabilization in superintense external fields [54]. We note that the vector potential (38) satisfies the zero-net-displacement condition (see, for example, the review [55] and references therein)

$$\int_{-\infty}^{\infty} dt A(t) = 0, \tag{42}$$

which favors stabilization. If the external field is superstrong, the electron moves like a free particle in the electromagnetic field during most of the pulse duration. Then if Eq. (42) holds, the final position of the electron is near the nucleus, and it has more chance of being recaptured in a bound state [54].

In the set of hydrogenlike ions with the scaled field parameters, the dipole ionization probabilities are equal to each other with a good accuracy in the weak-field region, until the local maximum of the probability is reached. Then the dynamic relativistic effects show up, making the ions with higher nuclear charge more stable against ionization [34]. When the external field is not very strong, the dipole and nondipole ionization probabilities agree very well. However, increasing the external field strength will eventually lead to a failure of the dipole approximation. As one can see in Fig. 1, the higher the nuclear charge, the weaker the scaled field where the dipole approximation breaks down. This is not surprising. The breakdown of the dipole approximation is mainly caused by the magnetic force of the external electromagnetic field. The nondipole corrections due to the magnetic field have the order of v/c, where v is a characteristic electron velocity; they are much larger than the dynamic relativistic effects such as the mass correction, which are proportional to $(v/c)^2$. This issue has been widely discussed in the literature (see, for example, Refs. [23–26,56,57]). The vector potential (37) beyond the dipole approximation, which depends on the variable

$$\eta = \omega t - \frac{\omega x}{c}, \tag{43}$$

violates invariance with respect to the nonrelativistic scaling (39) even if the system is treated nonrelativistically by the TDSE. Upon the scaling transformation (39), the temporal part ωt of this variable is invariant, while the spatial part $(\omega/c)x$ is multiplied by Z. Therefore, in the set of the hydrogenlike ions with the scaled external field parameters, one can expect more significant nondipole effects for the ions with the larger nuclear charge Z. As one can see in Fig. 1, the nondipole corrections in the ionization probability do not favor stabilization in superstrong fields. For He^+, the stabilization region is smaller than that for the hydrogen atom; for Ne^{9+}, this region almost disappears. Taking the 10% difference between the dipole and nondipole ionization probabilities as an indicator of the breakdown of the dipole approximation, we can find the corresponding scaled peak field values for the targets and pulse durations used in our calculations. These values are listed in Table I; they confirm that the dipole approximation fails at lower scaled peak field strengths for the targets with higher nuclear charge. Regarding the dependence on the pulse duration, one can see for H and He^+ that shorter pulse duration extends the validity region of the dipole approximation to stronger fields. This tendency is reversed for Ne^{9+}; for this ion with the relatively high nuclear charge, however, the dependence on the pulse duration is weak since the difference between the dipole and

TABLE I. Scaled peak field strength FZ^{-3} where the difference between the dipole and nondipole ionization probabilities reaches 10%.

	FZ^{-3} (a.u.)	
Target	$\tau = 2.5$ o.c.	$\tau = 3.75$ o.c.
H	64.7	50.4
He^+	41.5	35.8
Ne^{9+}	15.4	17.3

TABLE II. The parameters $Z\beta_0$ and Γ_R at the end of the dipole region as suggested by the peak field strengths in Table I.

	$Z\beta_0$		Γ_R	
Target	$\tau = 2.5$ o.c.	$\tau = 3.75$ o.c.	$\tau = 2.5$ o.c.	$\tau = 3.75$ o.c.
H	0.09	0.05	0.006	0.003
He^+	0.07	0.05	0.006	0.004
Ne^{9+}	0.05	0.06	0.008	0.011

nondipole ionization probabilities grows rapidly irrespective of the pulse duration after the peak field corresponding to the local maximum of the dipole ionization probability is passed.

As it was already mentioned, the nondipole effects in the ionization of hydrogenlike ions in strong electromagnetic fields are mainly caused by the influence of the magnetic force of the external field. Two different parameters have been introduced so far in the literature to measure the influence of the magnetic field and set the boundaries for validity of the dipole approximation. One approach [23–25] refers to the motion of a free electron in the field of the plane electromagnetic wave. The electron follows the so-called figure-eight trajectory [36] with the long axis along the polarization direction and short axis along the propagation direction of the wave. The extent of the trajectory in the propagation direction,

$$\beta_0 = \frac{U_p}{2\omega c}, \tag{44}$$

is due to the magnetic force [$U_p = F^2/(4\omega^2)$ is the ponderomotive potential of the external field]. The nondipole effects may be regarded insignificant if β_0 is much less than the first Bohr radius. This radius can be estimated as $1/\sqrt{2I_p}$, where I_p is the ionization potential. For hydrogenlike ions, the first Bohr radius is equal to the inverse nuclear charge Z^{-1}. Then we arrive at the following condition for applicability of the dipole approximation:

$$\sqrt{2I_p}\beta_0 = Z\beta_0 \ll 1. \tag{45}$$

Another approach [56,57] makes use of the Lorentz deflection parameter:

$$\Gamma_R = \frac{\sqrt{2I_p U_p^3}}{2\omega c^2}. \tag{46}$$

If $\Gamma_R \geqslant 1$, then the rescattering electron misses the parent ion due to deflection by the magnetic force, thus manifesting a failure of the traditional rescattering picture based on the dipole approximation. Therefore, it is expected that the dipole approximation works well if

$$\Gamma_R \ll 1. \tag{47}$$

We note that both $Z\beta_0$ and Γ_R parameters refer to an event within one optical cycle and thus do not depend on the pulse duration. One may expect that the deflection effect due to the magnetic field is more significant for longer pulses. As the results in Table I suggest, this is the case for small nuclear charges, and the applicability region of the dipole approximation does depend on the pulse duration. In our previous study [34], we calculated Γ_R for the laser pulse with $\tau = 2.5$ o.c. and found that the dipole approximation is valid if Γ_R is of the order of 10^{-3} or less. Here we present the data for both $Z\beta_0$ and Γ_R calculated for the pulse duration parameters $\tau = 2.5$ o.c. and $\tau = 3.75$ o.c. at the peak field strengths in Table I where a transition between the dipole and nondipole ionization regimes takes place. The results are listed in Table II. Generally, all the data in Table II satisfy conditions (45) and (47) with Γ_R being about ten times smaller than $Z\beta_0$. In a set of the hydrogenlike targets, $Z\beta_0$ seems to be more consistent for the pulse duration $\tau = 3.75$ o.c. while Γ_R is better at $\tau = 2.5$ o.c. At $\tau = 3.75$ o.c., however, the Γ_R value for Ne^{9+} is more than three times larger than that for the hydrogen atom. We should note, however, that the parameter Γ_R was derived [56] for the tunneling ionization regime and its applicability to the present case where the carrier frequency exceeds the ionization potential was not previously verified. Anyway, the values in Table II can help to estimate the range of both $Z\beta_0$ and Γ_R parameters where the dipole approximation can be safely used for the ionization probability calculations in the present case of superstrong high-frequency electromagnetic fields.

B. Energy and angular distributions of outgoing electrons

The photoelectron distributions with respect to their energies and emission angles are obtained by projecting the time-dependent wave function at the end of the pulse onto the continuum states with proper asymptotic behavior at large distances (plane wave plus incoming spherical wave). For the Coulomb potential, such continuum states are known in the analytic form [36]. For the chosen energy and emission angle, two different continuum states can be constructed corresponding to the spin projections $m_s = 1/2$ and $m_s = -1/2$ of the electron at rest [36]. In our TDDE calculations, the initial state is the ground state with $m = 0$; in the nonrelativistic limit, it means the spin projection is equal to 1/2. Then the projection of the final wave function onto the continuum state with $m_s = -1/2$ gives the probability amplitude of the spin-flip transition. For the light hydrogenlike targets and energy range near the ionization threshold, the spin-flip ionization probabilities are very small, several orders of magnitude less than the ionization probabilities without the spin flip [16]. Below we report the photoelectron distributions without spin selection, which include both $m_s = 1/2$ and $m_s = -1/2$ contributions. For all hydrogenlike targets with the scaled laser field parameters, the electron spectra after ionization manifest similar features, and the nondipole effects become more

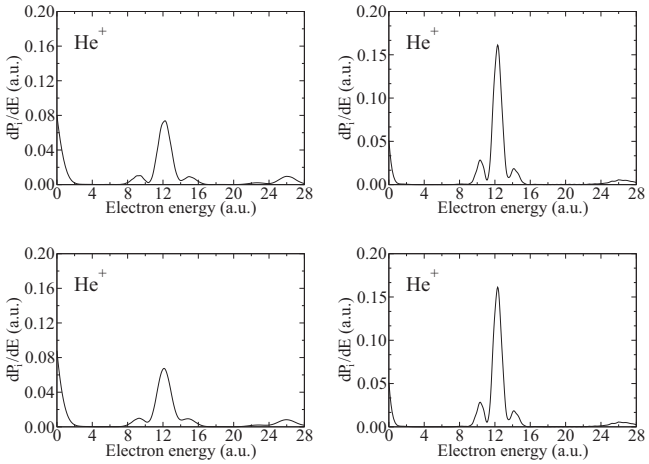

FIG. 2. Energy distributions of outgoing electrons after ionization of He^+ at the peak field strength $F = 20Z^3$ a.u. Left column, pulse duration $\tau = 2.5$ o.c.; right column, pulse duration $\tau = 3.75$ o.c. Top row, dipole approximation; bottom row, beyond the dipole approximation. The carrier frequency is $\omega = 3.5Z^2$ a.u.

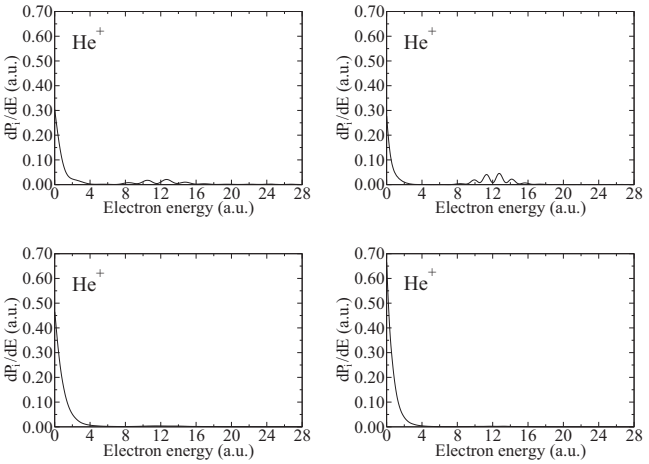

FIG. 4. Energy distributions of outgoing electrons after ionization of He^+ at the peak field strength $F = 60Z^3$ a.u. Left column, pulse duration $\tau = 2.5$ o.c.; right column, pulse duration $\tau = 3.75$ o.c. Top row, dipole approximation; bottom row, beyond the dipole approximation. The carrier frequency is $\omega = 3.5Z^2$ a.u.

pronounced with increasing the nuclear charge Z. Here we present the results for He^+ ion.

In Figs. 2–4, the angle-integrated energy distribution (ionization probability per unit energy interval, dP_i/dE) is shown for the peak field strengths $20Z^3$ a.u., $40Z^3$ a.u., and $60Z^3$ a.u., respectively. In each figure, one can compare the spectra with the pulse durations $\tau = 2.5$ o.c. and $\tau = 3.75$ o.c. obtained both within and beyond the dipole approximation. We can confirm the conclusion made in Ref. [16] that the nondipole effects become more important for stronger laser fields. At relatively weak peak field $F = 20Z^3$ a.u. (Fig. 2), there is no qualitative difference between the dipole and nondipole spectra. There is a prominent above-threshold ionization (ATI) peak located approximately at the energy $E_1 = 12$ a.u. and corresponding to absorption of one photon as well as a weaker two-photon ATI peak at $E_2 = 26$ a.u. Note that the peak positions E_n in the spectrum follow closely the energy conservation relation

$$E_n = E_0 + n\omega, \tag{48}$$

where E_0 is the *unperturbed* ground-state energy and n is the number of absorbed photons. This equation does not contain the ac Stark shift of the ground energy level and ponderomotive potential U_p, which usually plays a key role in the ATI processes causing, for example, the famous peak switching in strong laser fields [58]. In the present case, however, the external field is not strong but superstrong, equally perturbing bound and continuum states and shifting them all by the same amount U_p (for the field parameters in Fig. 2, $U_p = 32.65$ a.u.). Hence the ionization potential does not change, and the ATI peak positions are determined by Eq. (48). It means the ATI peaks are not shifted by the ponderomotive potential [59], demonstrating the same behavior as in the opposite case of weak fields.

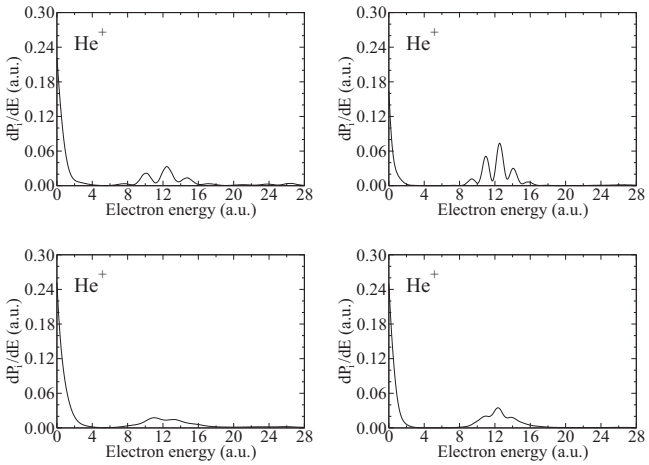

FIG. 3. Energy distributions of outgoing electrons after ionization of He^+ at the peak field strength $F = 40Z^3$ a.u. Left column, pulse duration $\tau = 2.5$ o.c.; right column, pulse duration $\tau = 3.75$ o.c. Top row, dipole approximation; bottom row, beyond the dipole approximation. The carrier frequency is $\omega = 3.5Z^2$ a.u.

The widths of the ATI peaks are due to the finite duration of the laser pulse. The spectral width of the Gaussian pulse in the frequency domain is inversely proportional to the parameter τ, so the shorter the pulse, the wider the ATI peaks. This is clearly seen in Fig. 2: in the right column ($\tau = 3.75$ o.c.), the first ATI peak is narrower and higher than that in the left column ($\tau = 2.5$ o.c.). One can also see that the main ATI peak has a satellite peak structure with the subpeaks located both on the left and on the right of the main peak. This satellite peak structure is not related to the structures in the ATI spectra due to interference of the contributions to the ionization amplitude from the raising and falling edges of the laser pulse [60,61]. The structure discussed here exists in a very strong external field and is caused by the interference of different order contributions to the ionization amplitude in a nonmonochromatic field. For the first ATI peak, such contributions represent first and third orders of the perturbation theory with respect to the external field, at least. The phase

difference between the contributions is proportional to the energy E and pulse duration τ, so the oscillation period in the interference pattern on the energy scale is larger for shorter pulse, as seen in Fig. 2. The interference structure shows up if the external field is strong enough and high-order contributions to the ionization amplitude are comparable in magnitude with the one-photon contribution. As the calculations confirm, it disappears if the peak field strength falls below $5Z^3$ a.u. Finally, one can see a low-energy structure close to the ionization threshold in the energy spectra of Fig. 2. We note that this low-energy structure (LES) is different from the original LES observed in ATI experiments with mid-infrared laser fields [62,63] and explained by the Coulomb focusing and rescattering effects [64–66] (see also Refs. [67–69]). In our case, the LES results from multiphoton absorption-emission processes in a nonmonochromatic external field. At least absorption of one photon in the high-energy part of the pulse frequency spectrum and emission of one photon in the low-energy part of this spectrum is required for the electron to reach the final energy near the threshold. Then the LES must become more pronounced if the pulse duration decreases (that is, the range in the frequency domain, where the field components have comparable amplitudes, increases). This is confirmed by the energy spectra in Fig. 2, if one compares the results for the pulse duration $\tau = 3.75$ o.c. and $\tau = 2.5$ o.c.: the LES is stronger for the shorter pulse.

On the other hand, compared to the first ATI peak, the LES builds up as the peak field strength increases. It happens because this structure emerges from the second- and higher-order processes while the ATI peak is dominated by the one-photon absorption. These considerations are confirmed by our calculations presented in Figs. 3 and 4. At $F = 40Z^3$ a.u. the LES dominates both the dipole and nondipole energy spectra while the ATI peak becomes lower and wider, and at $F = 60Z^3$ a.u. the ATI peak almost totally disappears. The differences between the dipole and nondipole energy distributions are clearly seen in more intense fields. Generally, the LES is even stronger and the ATI peak is weaker in the nondipole spectra. Besides that, the interference pattern in the nondipole ATI peak is largely washed out.

In Figs. 5–7, we show the 2D energy-angle pseudocolor plots of photoelectron spectra for the same peak fields and pulse durations as in Figs. 2–4. They represent the cross sections of the electron distributions in either x-z or y-z plane. The laser pulse is polarized in the z direction (vertical axis in all figures) and propagates in the positive x direction. The radial distance in Figs. 5–7 measures the electron kinetic energy, and deflection from the positive z axis determines the polar angle ϑ of the ejected electron. The ionization probability density is represented on a linear pseudocolor scale. The top row plots in all the figures display the energy-angle spectra in the dipole approximation. Within the dipole approximation, the photoelectron distributions do not depend on the azimuthal angle φ, so only the x-z cross section is shown. As expected, both in the LES and the first ATI peak, the electrons are ejected predominantly in the polarization (z) direction. The ATI peak exhibits a deep minimum in the perpendicular direction, although the angular distribution is rather wide. In the superstrong laser fields, the first ATI peak is not described by the the first-order transition amplitude with the angular distribution proportional

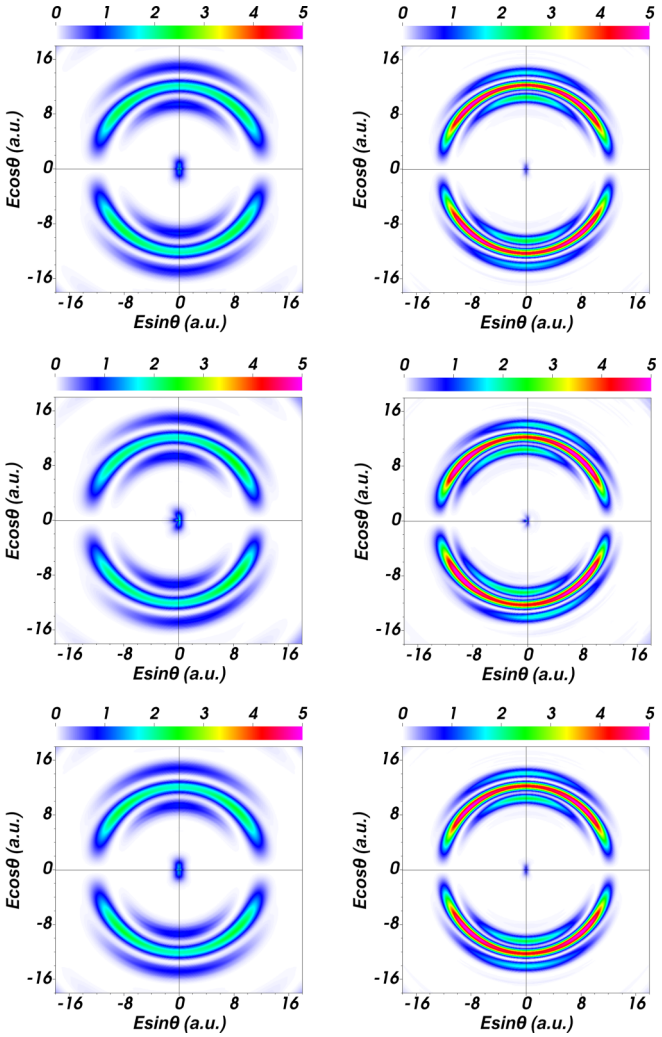

FIG. 5. Energy-angle differential ionization probabilities of He^+ at the peak field strength $F = 20Z^3$ a.u. Left column, pulse duration $\tau = 2.5$ o.c.; right column, pulse duration $\tau = 3.75$ o.c. Top row, dipole approximation; middle row, distribution in the x-z plane; bottom row, distribution in the y-z plane. The density (color) scale is linear, and the units are arbitrary. The carrier frequency is $\omega = 3.5Z^2$ a.u.

to $\cos^2\vartheta$. As one can see in Figs. 5–7, the angular dependence in the ATI peak may have local maxima not in the z direction, which originate from the high-order contributions to the ionization amplitude. We note again that the photoelectron angular distributions in the dipole approximations possess the rotational symmetry about the z axis, so the dipole plots in Figs. 5–7 exhibit the left-right reflection symmetry. However, there is no strict forward-backward symmetry in the z direction for the pulsed fields. In the same dipole plots, one can notice slight differences between the spectra in the upper and lower half planes.

Beyond the dipole approximation, the rotational symmetry about the z axis is broken in the angular distributions. Since the magnetic field of the pulse is directed along the y axis, it may push the outgoing electron in the x direction, provided the initial electron velocity is parallel to the field polarization (z) axis. Consequently, a left-right asymmetry of the energy-

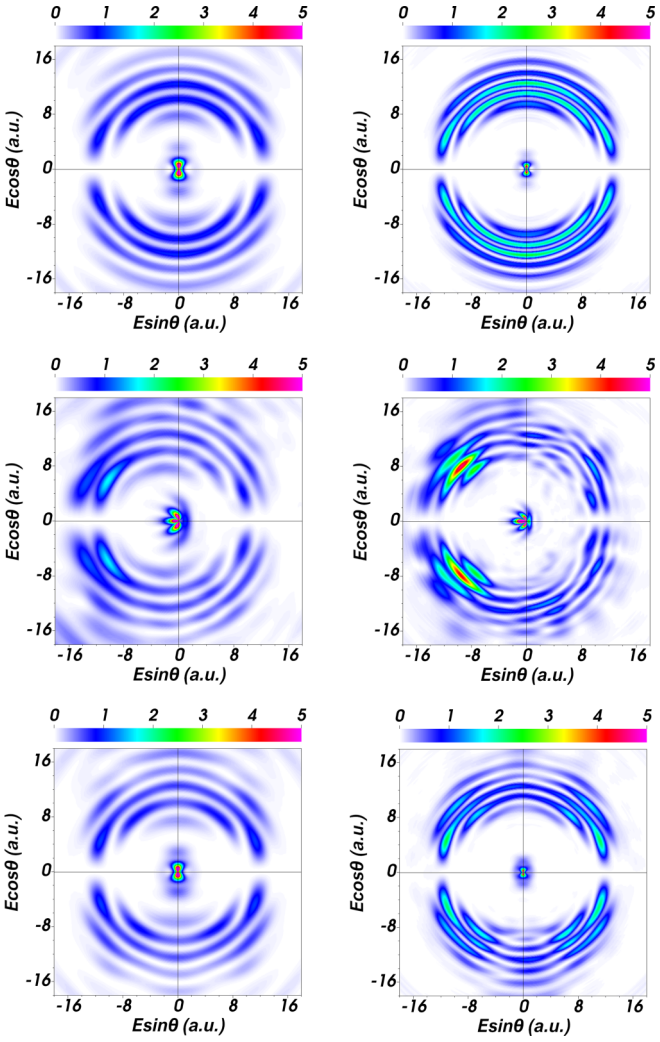

FIG. 6. Energy-angle differential ionization probabilities of He^+ at the peak field strength $F = 40Z^3$ a.u. Left column, pulse duration $\tau = 2.5$ o.c.; right column, pulse duration $\tau = 3.75$ o.c. Top row, dipole approximation; middle row, distribution in the x-z plane; bottom row, distribution in the y-z plane. The density (color) scale is linear, and the units are arbitrary. The carrier frequency is $\omega = 3.5Z^2$ a.u.

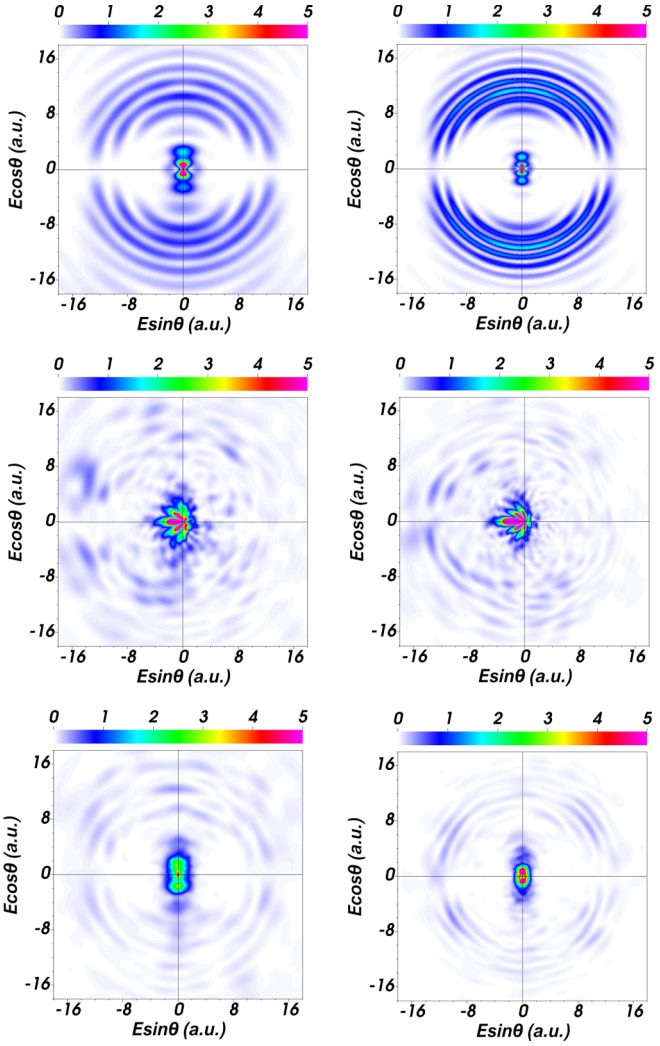

FIG. 7. Energy-angle differential ionization probabilities of He^+ at the peak field strength $F = 60Z^3$ a.u. Left column, pulse duration $\tau = 2.5$ o.c.; right column, pulse duration $\tau = 3.75$ o.c. Top row, dipole approximation; middle row, distribution in the x-z plane; bottom row, distribution in the y-z plane. The density (color) scale is linear, and the units are arbitrary. The carrier frequency is $\omega = 3.5Z^2$ a.u.

angle distributions must show up in the x-z plane while the spectra in the y-z plane remain symmetric. This asymmetry is already visible at $F = 20Z^3$ a.u. (Fig. 5), although the angle-integrated energy spectrum differs very little from that in the dipole approximation (Fig. 2). As the peak field increases, the left-right asymmetry of the energy-angle distributions in the x-z plane becomes stronger. In average, the outgoing electrons are pushed in the negative x direction, that is, *opposite* to the propagation direction of the electromagnetic wave. This effect was previously revealed in the nonrelativistic calculations of photoionization of the hydrogen atom beyond the dipole approximation [29]. As our results show, it can be observed in both the LES and the ATI peak in stronger fields $F = 40Z^3$ a.u. and $F = 60Z^3$ a.u. (Figs. 6 and 7). However, at $F = 20Z^3$ a.u. (Fig. 5) different energy components (rings) in the ATI peak have their largest intensities in different (left and right) half planes in the x-z plane. It means the combined effect of the Coulomb and external electromagnetic field beyond the dipole approximation (at least, in weaker external fields) may push the ejected electrons not only backward but also forward with respect to the propagation direction. Another nondipole effect in the ATI peak, most clearly seen at $F = 40Z^3$ a.u. (Fig. 6), is as follows: the electrons initially ejected in the right x-z half plane are decelerated and those ejected in the left x-z half plane are accelerated by the combined Coulomb and external electromagnetic field. Thus the final kinetic energy of the electron in the same ring within the ATI peak is larger in the left half plane and smaller in the right half plane.

Regarding the LES, its energy-angle distribution within the dipole approximation is stretched along the z axis. If the nondipole corrections are included, the ends of this distribution are bent in the negative x direction. A characteristic feature of the LES beyond the dipole approximation is a

lobe in the angular distributions along the x axis opposite to the propagation direction of the pulse [29]. One can see in Figs. 5–7 that this lobe builds up as the peak field strength increases. At the weaker peak field $F = 20Z^3$ a.u., the nondipole distribution has a three-lobe shape: one lobe along the x axis and two side lobes pointing at some directions in the left x-z half plane. As the peak field gets stronger, the shape of the distribution becomes more complex, and the number of side lobes increases. This is clearly seen in Figs. 6 and 7.

The energy-angle distributions in the y-z plane preserve the left-right symmetry beyond the dipole approximation, as it was already mentioned. One can see these spectra in the bottom rows of Figs. 5–7. For the ATI peak, the main nondipole effect here is that the maximum of the probability density moves away from the polarization direction (z axis). One can see it at $F = 40Z^3$ a.u. in Fig. 6 where the ATI peak is still strong enough. At $F = 60Z^3$ a.u. (Fig. 7) the tendency is the same with the probability density maxima shifted towards the y axis, but the probability density itself is very low in the ATI peak compared to the LES. In the LES itself, the energy-angle distribution is stretched along the z axis but its shape differs significantly from that in the dipole approximation.

IV. CONCLUSION

In this paper, we have performed a relativistic study of hydrogenlike ions in superstrong linearly polarized pulsed electromagnetic fields. To solve both the time-independent and time-dependent Dirac equations, we apply the generalized pseudospectral method in spherical coordinates. We suggest a transformation of the radial Dirac Hamiltonian in the spirit of the dual kinetic balance approach that removes the spurious eigenstates, which usually show up when solving the Dirac equation with the help of basis set expansions. The time propagation is accomplished through the radial 1D propagators, thus dramatically reducing the computational effort as compared to our previous 2D implementation [34].

The ionization probabilities have been calculated for the hydrogen atom as well as hydrogenlike helium and neon. For He^+ and Ne^{9+}, the external field parameters such as the peak field strength, carrier frequency, and pulse duration are scaled with respect to the nuclear charge, so all three hydrogenlike targets have identical ionization probabilities if being treated nonrelativistically by the TDSE within the dipole approximation. Then the deviation from the scaling law can be attributed to relativistic and nondipole effects. For the light hydrogenlike ions and field parameters used in the calculations, the key role is played by the nondipole effects rather than kinematic relativistic corrections. As expected, the nondipole effects are more important for stronger external fields. The pattern in the dependence of the ionization probability on the peak field strength beyond the dipole approximation differs qualitatively from that in the dipole approximation: instead of relative stabilization in strong fields observed in the dipole approximation, the nondipole ionization probability increases with the field strength. In the set of the hydrogenlike ions with scaled external field parameters, the nondipole corrections to the ionization probabilities are larger for the targets with higher nuclear charges.

Having at hand both the dipole and nondipole numerical data for the ionization probability, we can determine the validity limits of the dipole approximation. Based on this analysis, we set the range for the analytic parameters, previously suggested in the literature to estimate the nondipole effects. These parameters depend on the strength and carrier frequency of the external field but do not depend on the pulse duration. We find that validity of the dipole approximation does depend on the pulse duration: for the first two targets, H and He^+, and two pulse durations used in our calculations, the nondipole effects appear more significant for the longer pulse. However, this is not the case for the ion with higher nuclear charge, Ne^+. Certainly, the pulse duration effect on the validity of the dipole approximation deserves further investigation.

The photoelectron energy spectra after ionization in superstrong fields manifest the features which are not so prominent in weaker fields: the satellite structure in the ATI peaks and the LES. With increasing the peak field strength, the LES builds up while the ATI peaks decrease. The nondipole effects in the energy-angle distributions break the rotational symmetry about the polarization direction of the electromagnetic field. Generally, the distributions are pushed in the hemisphere opposite to the propagation direction of the electromagnetic wave, although some energy components of the spectra may show a stronger signal in the hemisphere along the propagation direction, if the external field is relatively weak. In the angular distributions within the LES, a prominent lobe opposite to the propagation direction shows up and becomes dominant in stronger fields.

ACKNOWLEDGMENTS

D.A.T. acknowledges the support from the RFBR (Grant No. 20-02-00199) and RFBR and ROSATOM (Grant No. 20-21-00098). This work was also partially supported by the Ministry of Science and Technology of Taiwan and National Taiwan University (Grants No. 109L892001 and No. 109L104048).

[1] F. Krausz and M. Ivanov, Attosecond physics, Rev. Mod. Phys. **81**, 163 (2009).

[2] A. Di Piazza, C. Müller, K. Z. Hatsagortsyan, and C. H. Keitel, Extremely high-intensity laser interactions with fundamental quantum systems, Rev. Mod. Phys. **84**, 1177 (2012).

[3] T. Tschentscher and R. Feidenhans'l, Starting user operation at the European XFEL, Synchrotron Radiat. News **30**, 21 (2017).

[4] M. Dunne and B. Schoenlein, The Linac Coherent Light Source: Current status and future direction, Synchrotron Radiat. News **30**, 7 (2017).

[5] S. Selstø, E. Lindroth, and J. Bengtsson, Solution of the Dirac equation for hydrogenlike systems exposed to intense electromagnetic pulses, Phys. Rev. A **79**, 043418 (2009).

[6] Y. V. Vanne and A. Saenz, Solution of the time-dependent Dirac equation for multiphoton ionization of highly charged hydrogenlike ions, Phys. Rev. A **85**, 033411 (2012).

[7] A. S. Simonsen, T. Kjellsson, M. Førre, E. Lindroth, and S. Selstø, Ionization dynamics beyond the dipole approximation induced by the pulse envelope, Phys. Rev. A **93**, 053411 (2016).

[8] T. Kjellsson, S. Selstø, and E. Lindroth, Relativistic ionization dynamics for a hydrogen atom exposed to superintense XUV laser pulses, Phys. Rev. A **95**, 043403 (2017).

[9] T. Kjellsson, M. Førre, A. S. Simonsen, S. Selstø, and E. Lindroth, Alternative gauge for the description of the light-matter interaction in a relativistic framework, Phys. Rev. A **96**, 023426 (2017).

[10] I. V. Ivanova, V. M. Shabaev, D. A. Telnov, and A. Saenz, Scaling relations of the time-dependent dirac equation describing multiphoton ionization of hydrogenlike ions, Phys. Rev. A **98**, 063402 (2018).

[11] X.-M. Tong and Shih-I Chu, Relativistic density-functional theory with the optimized effective potential and self-interaction correction: Application to atomic structure calculations ($Z =$ 2–106), Phys. Rev. A **57**, 855 (1998).

[12] E. B. Rozenbaum, D. A. Glazov, V. M. Shabaev, K. E. Sosnova, and D. A. Telnov, Dual-kinetic-balance approach to the Dirac equation for axially symmetric systems: Application to static and time-dependent fields, Phys. Rev. A **89**, 012514 (2014).

[13] M. S. Pindzola, J. A. Ludlow, and J. Colgan, Photoionization of highly charged atomic ions, Phys. Rev. A **81**, 063431 (2010).

[14] M. S. Pindzola, S. A. Abdel-Naby, F. Robicheaux, and J. Colgan, Single photoionization of highly charged atomic ions including the full electromagnetic-field potential, Phys. Rev. A **85**, 032701 (2012).

[15] I. A. Ivanov, Relativistic calculation of the electron-momentum shift in tunneling ionization, Phys. Rev. A **91**, 043410 (2015).

[16] I. A. Ivanov, Spin-flip processes and nondipole effects in above-threshold ionization of hydrogen in ultrastrong laser fields, Phys. Rev. A **96**, 013419 (2017).

[17] H. Bauke, H. G. Hetzheim, G. R. Mocken, M. Ruf, and C. H. Keitel, Relativistic ionization characteristics of laser-driven hydrogenlike ions, Phys. Rev. A **83**, 063414 (2011).

[18] M. Klaiber, E. Yakaboylu, C. Müller, H. Bauke, G. G. Paulus, and K. Z. Hatsagortsyan, Spin dynamics in relativistic ionization with highly charged ions in super-strong laser fields, J. Phys. B **47**, 065603 (2014).

[19] M. Klaiber and K. Z. Hatsagortsyan, Spin-asymmetric laser-driven relativistic tunneling from p states, Phys. Rev. A **90**, 063416 (2014).

[20] T. K. Lindblom, M. Førre, E. Lindroth, and S. Selstø, Semirelativistic Schrödinger Equation for Relativistic Laser-Matter Interactions, Phys. Rev. Lett. **121**, 253202 (2018).

[21] M. Førre, Breakdown of the nonrelativistic approximation in superintense laser-matter interactions, Phys. Rev. A **99**, 053410 (2019).

[22] M. Førre and S. Selstø, Schrödinger formulation of the nondipole light-matter interaction consistent with relativity, Phys. Rev. A **101**, 063416 (2020).

[23] H. R. Reiss, Dipole-approximation magnetic fields in strong laser beams, Phys. Rev. A **63**, 013409 (2000).

[24] H. R. Reiss, Limits on Tunneling Theories of Strong-Field Ionization, Phys. Rev. Lett. **101**, 043002 (2008).

[25] H. R. Reiss, The tunnelling model of laser-induced ionization and its failure at low frequencies, J. Phys. B **47**, 204006 (2014).

[26] A. Ludwig, J. Maurer, B. W. Mayer, C. R. Phillips, L. Gallmann, and U. Keller, Breakdown of the Dipole Approximation in Strong-Field Ionization, Phys. Rev. Lett. **113**, 243001 (2014).

[27] J. Daněk, M. Klaiber, K. Z. Hatsagortsyan, C. H. Keitel, B. Willenberg, J. Maurer, B. W. Mayer, C. R. Phillips, L. Gallmann, and U. Keller, Interplay between Coulomb-focusing and non-dipole effects in strong-field ionization with elliptical polarization, J. Phys. B **51**, 114001 (2018).

[28] N. Haram, I. Ivanov, H. Xu, K. T. Kim, A. Atia-tul Noor, U. S. Sainadh, R. D. Glover, D. Chetty, I. V. Litvinyuk, and R. T. Sang, Relativistic Nondipole Effects in Strong-Field Atomic Ionization at Moderate Intensities, Phys. Rev. Lett. **123**, 093201 (2019).

[29] M. Førre, J. P. Hansen, L. Kocbach, S. Selstø, and L. B. Madsen, Nondipole Ionization Dynamics of Atoms in Superintense High-Frequency Attosecond Pulses, Phys. Rev. Lett. **97**, 043601 (2006).

[30] M. Førre, S. Selstø, J. P. Hansen, T. K. Kjeldsen, and L. B. Madsen, Molecules in intense xuv pulses: Beyond the dipole approximation in linearly and circularly polarized fields, Phys. Rev. A **76**, 033415 (2007).

[31] Z. Zhou and Shih-I Chu, Multiphoton above-threshold ionization in superintense free-electron x-ray laser fields: Beyond the dipole approximation, Phys. Rev. A **87**, 023407 (2013).

[32] T. E. Moe and M. Førre, Ionization of atomic hydrogen by an intense x-ray laser pulse: An *ab initio* study of the breakdown of the dipole approximation, Phys. Rev. A **97**, 013415 (2018).

[33] D. A. Telnov, D. A. Krapivin, J. Heslar, and S.-I. Chu, Multiphoton ionization of one-electron relativistic diatomic quasimolecules in strong laser fields, J. Phys. Chem. A **122**, 8026 (2018).

[34] D. A. Telnov and Shih-I Chu, Relativistic ionization dynamics of hydrogenlike ions in strong electromagnetic fields: Generalized pseudospectral method for the time-dependent Dirac equation, Phys. Rev. A **102**, 063109 (2020).

[35] S.-I. Chu and D. A. Telnov, Beyond the Floquet theorem: Generalized Floquet formalisms and quasienergy methods for atomic and molecular multiphoton processes in intense laser fields, Phys. Rep. **390**, 1 (2004).

[36] V. B. Berestetskii, E. M. Lifshitz, and L. P. Pitaevskii, *Quantum Electrodynamics*, 2nd ed. (Pergamon Press, Oxford, 1982).

[37] D. A. Varshalovich, A. N. Moskalev, and V. K. Khersonskii, *Quantum Theory of Angular Momentum* (World Scientific, Singapore, 1988).

[38] X.-M. Tong and S.-I. Chu, Theoretical study of multiple high-order harmonic generation by intense ultrashort pulsed laser fields: A new generalized pseudospectral time-dependent method, Chem. Phys. **217**, 119 (1997).

[39] D. A. Telnov and S.-I. Chu, Time-dependent generalized pseudospectral method for accurate treatment of multiphoton processes of diatomic molecules in intense laser fields, Comput. Phys. Commun. **182**, 18 (2011).

[40] D. A. Telnov, J. Heslar, and Shih-I Chu, Effects of nuclear vibration on high-order-harmonic generation of aligned H_2^+ molecules, Phys. Rev. A **90**, 063412 (2014).

[41] D. A. Telnov and Shih-I Chu, Minima in low-energy above-threshold-ionization spectra induced by electronic structure, Phys. Rev. A **100**, 043423 (2019).

[42] D. A. Telnov, J. Heslar, and S.-I. Chu, Strong-field ionization of Li and Be: A time-dependent density functional theory with self-interaction correction, Chem. Phys. **391**, 88 (2011).

[43] D. A. Telnov, K. E. Sosnova, E. Rozenbaum, and Shih-I Chu, Exterior complex scaling method in time-dependent

density-functional theory: Multiphoton ionization and high-order-harmonic generation of Ar atoms, Phys. Rev. A **87**, 053406 (2013).

[44] K. Nasiri Avanaki, D. A. Telnov, and Shih-I Chu, Harmonic generation of Li atoms in one- and two-photon Rabi-flopping regimes, Phys. Rev. A **94**, 053410 (2016).

[45] Y. Salamin, S. Hu, K. Hatsagortsyan, and C. Keitel, Relativistic high-power laser-matter interactions, Phys. Rep. **427**, 41 (2006).

[46] I. P. Grant, B-spline methods for radial Dirac equations, J. Phys. B **42**, 055002 (2009).

[47] W. R. Johnson, S. A. Blundell, and J. Sapirstein, Finite basis sets for the Dirac equation constructed from *B* splines, Phys. Rev. A **37**, 307 (1988).

[48] E. Layton and Shih-I Chu, Generalized Fourier-grid Hamiltonian approach to the Dirac equation: Variational solution without basis set, Chem. Phys. Lett. **186**, 100 (1991).

[49] V. M. Shabaev, I. I. Tupitsyn, V. A. Yerokhin, G. Plunien, and G. Soff, Dual Kinetic Balance Approach to Basis-Set Expansions for the Dirac Equation, Phys. Rev. Lett. **93**, 130405 (2004).

[50] C. Froese Fischer and O. Zatsarinny, A B-spline Galerkin method for the Dirac equation, Comput. Phys. Commun. **180**, 879 (2009).

[51] F. Fillion-Gourdeau, E. Lorin, and A. D. Bandrauk, Numerical solution of the time-independent Dirac equation for diatomic molecules: *B* splines without spurious states, Phys. Rev. A **85**, 022506 (2012).

[52] Q. Z. Lv, S. Norris, Q. Su, and R. Grobe, Numerical split-shift potential method for relativistic quantum systems with radial symmetry, J. Phys. B **49**, 065003 (2016).

[53] L. B. Madsen and P. Lambropoulos, Scaling of hydrogenic atoms and ions interacting with laser fields: Positronium in a laser field, Phys. Rev. A **59**, 4574 (1999).

[54] M. Gavrila, Atomic stabilization in superintense laser fields, J. Phys. B **35**, R147 (2002).

[55] D. B. Milošević, G. G. Paulus, D. Bauer, and W. Becker, Above-threshold ionization by few-cycle pulses, J. Phys. B **39**, R203 (2006).

[56] S. Palaniyappan, I. Ghebregziabher, A. DiChiara, J. MacDonald, and B. C. Walker, Emergence from nonrelativistic strong-field rescattering to ultrastrong-field laser-atom physics: A semiclassical analysis, Phys. Rev. A **74**, 033403 (2006).

[57] M. Klaiber, K. Z. Hatsagortsyan, J. Wu, S. S. Luo, P. Grugan, and B. C. Walker, Limits of Strong Field Rescattering in the Relativistic Regime, Phys. Rev. Lett. **118**, 093001 (2017).

[58] P. Kruit, J. Kimman, H. G. Muller, and M. J. van der Wiel, Electron spectra from multiphoton ionization of xenon at 1064, 532, and 355 nm, Phys. Rev. A **28**, 248 (1983).

[59] D. A. Tumakov, D. A. Telnov, G. Plunien, V. A. Zaytsev, and V. M. Shabaev, Relativistic mask method for electron momentum distributions after ionization of hydrogen-like ions in strong laser fields, Eur. Phys. J. D **74**, 188 (2020).

[60] V. C. Reed and K. Burnett, Role of resonances and quantum-mechanical interference in the generation of above-threshold-ionization spectra, Phys. Rev. A **43**, 6217 (1991).

[61] D. A. Telnov and Shih-I Chu, Multiphoton above-threshold detachment by intense laser pulses: a new adiabatic approach, J. Phys. B **28**, 2407 (1995).

[62] C. I. Blaga, F. Catoire, P. Colosimo, G. G. Paulus, H. G. Muller, P. Agostini, and L. F. DiMauro, Strong-field photoionization revisited, Nat. Phys. **5**, 335 (2009).

[63] W. Quan, Z. Lin, M. Wu, H. Kang, H. Liu, X. Liu, J. Chen, J. Liu, X. T. He, S. G. Chen, H. Xiong, L. Guo, H. Xu, Y. Fu, Y. Cheng, and Z. Z. Xu, Classical Aspects in Above-Threshold Ionization with a Midinfrared Strong Laser Field, Phys. Rev. Lett. **103**, 093001 (2009).

[64] C. Liu and K. Z. Hatsagortsyan, Origin of Unexpected Low Energy Structure in Photoelectron Spectra Induced by Mid-infrared Strong Laser Fields, Phys. Rev. Lett. **105**, 113003 (2010).

[65] T.-M. Yan, S. V. Popruzhenko, M. J. J. Vrakking, and D. Bauer, Low-Energy Structures in Strong Field Ionization Revealed by Quantum Orbits, Phys. Rev. Lett. **105**, 253002 (2010).

[66] A. Kästner, U. Saalmann, and J. M. Rost, Electron-Energy Bunching in Laser-Driven Soft Recollisions, Phys. Rev. Lett. **108**, 033201 (2012).

[67] D. A. Telnov and Shih-I Chu, Low-energy structure of above-threshold-ionization electron spectra: Role of the Coulomb threshold effect, Phys. Rev. A **83**, 063406 (2011).

[68] L. Guo, S. S. Han, X. Liu, Y. Cheng, Z. Z. Xu, J. Fan, J. Chen, S. G. Chen, W. Becker, C. I. Blaga, A. D. DiChiara, E. Sistrunk, P. Agostini, and L. F. DiMauro, Scaling of the Low-Energy Structure in Above-Threshold Ionization in the Tunneling Regime: Theory and Experiment, Phys. Rev. Lett. **110**, 013001 (2013).

[69] M. Möller, F. Meyer, A. M. Sayler, G. G. Paulus, M. F. Kling, B. E. Schmidt, W. Becker, and D. B. Milošević, Off-axis low-energy structures in above-threshold ionization, Phys. Rev. A **90**, 023412 (2014).